Materials International
Open-Access Journal (ISSN: 2668-5728)

Article
Volume 8, Issue 1, 2026, 1
https://doi.org/10.33263/Materials81.001

Green Synthesis of Co@α-Fe_2O_3 Nanoparticles and Structural Analysis via Rietveld Refinement

Soufiane Hmamouchi [1], Ahmed El Yacoubi [1,2,*], Mohamed Berradi [3], Mounir El Hezzat [1], Brahim Sallek [1], Brahim Chafik El Idrissi [1]

[1] Laboratory of Advanced Materials Engineering (LAME), Faculty of Sciences, Ibn Tofaïl University, Kenitra 14000, Morocco; brahim.chafikelidrissi@uit.ac.ma;
[2] Mineral Solid Chemistry team (MSCT), Laboratory of Applied Chemistry and Environment (LACE), Faculty of Sciences, Mohamed First University, Oujda 60000, Morocco; Ahmed.elyacoubi@uit.ac.ma;
[3] Laboratory of Organic Chemistry, Catalysis and Environment (LOC2E), Department of Chemistry, Faculty of Science, University Ibn Tofaïl, B.P.133, Kenitra, 14000, Morocco
* Correspondence: Ahmed.elyacoubi@uit.ac.com;

Received: 30.09.2025; Accepted: 20.02.2026; Published: 10.03.2026

Abstract: Cobalt-doped hematite (Co@α-Fe_2O_3) nanoparticles (NPs) with a crystallite size of 45 nm were successfully prepared using a cost-efficient and green approach involving Fe(III) and Co(II) chlorides and freshly separated hen egg white, followed by annealing and milling the powder at 550°C. The obtained powder was characterized by XRD, FTIR, and SEM/EDS analyses, and its structure was refined using Rietveld analysis. XRD results revealed the predominant formation of rhombohedral α-Fe_2O_3 (space group R-3c) with a minor γ- Fe_2O_3 secondary phase. Structural analysis confirms that the compound crystallizes in the rhombohedral unit cell of the corundum structure. Rietveld refinement confirmed high structural reliability (Rwp = 2.90, χ^2= 1.38) and yielded refined lattice parameters of a = b = 5.0326 Å and c = 13.7359 Å, indicating a slight lattice distortion associated with Co^{2+} substitution in octahedral Fe^{3+} sites. Bond length analysis revealed two distinct M–O distances (1.926 Å and 2.137 Å), reflecting octahedral distortion within the hematite structure. FTIR spectroscopic analysis indicated clear evidence for the formation of the Co@α-Fe_2O_3 phase. EDS findings confirm the presence of Fe and Co particles in the sample. The structure consists of Fe^{3+}(Co^{2+}) ions octahedrally coordinated with O^{2-} ions.

Keywords: Co@α-Fe_2O_3 nanoparticles; Co dopant; green synthesis; structural properties; Rietveld refinement.

1. Introduction

Nanoscale transition of metallic oxides has garnered growing interest in recent years, owing to their distinct and exceptional opto-electronic, photoluminescence, electrical, optical, and magnetic properties, making them suitable for a wide range of applications, including wastewater treatment, ferrofluid technology, solar cells, inorganic pigments, optical and electronic devices, photodetectors, spintronics, and the development of gas sensors, among others [1–3]. Among these materials, the n-type semiconductor hematite (Fe2O3) is an important transition-metal oxide due to its natural abundance, eco-friendliness, low cost, high stability, visible-ght harvesting ability, and notable electrochemical activity [4,5]. The doping

of metal ions significantly influences the chemical reactivity, morphology, particle size, and Fe_2O_3 redox behavior [6,7].

Fe_2O_3 crystallizes in four different allotropic varieties: α-, β-, γ-, and ε-Fe_2O_3 [8]. α-Fe_2O_3 is the most abundant in nature, commonly found in soils, sediments, and aquatic systems. The crystal structure of α- Fe_2O_3 crystallizes with two formula units per unit cell, adopting both primitive rhombohedral and trigonal–hexagonal unit cells (Figure 1) [9]. The arrangement of O and Fe atoms forms a trigonal–hexagonal lattice with the R-3c space group and lattice parameters a = b = 0.5034 nm, and c = 1.375 nm, with six formula units per unit cell. The unit-cell parameters of the rhombohedral structure are: α = 55.31° and a_{rh} = 0.5427 nm [10]. In the α- Fe_2O_3 lattice, the cations Fe^{3+} and the anions O^{2-} are arranged in a hexagonal close-packed lattice. The Fe^{3+} cations occupy 2/3 of the sites, creating 6-fold rings on the (001) plane where two sites are occupied and one is vacant [11].

The purpose of the present work was to perform an XRD study of Co@α-Fe_2O_3 iron oxide nanoparticles prepared by an aqueous coprecipitation method using hen egg white albumin and to investigate the effect of Cobalt incorporation on the structure of α-Fe_2O_3 s using the Rietveld method with the free Fullprof-suite software. The structural properties of the obtained nanopowders were investigated using Fourier-transformed infrared spectroscopy (FTIR), X-ray powder diffraction analysis (XRD), and a field-emission scanning electron microscope equipped with energy-dispersive X-ray spectroscopy (SEM/EDX).

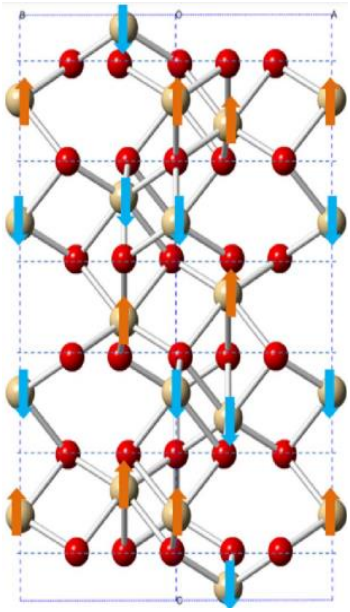

Figure 1. Hexagonal α-Fe_2O_3 lattice. Iron and oxygen atoms are represented by large and small balls, respectively [9].

2. Materials and Methods

All chemicals obtained from Sigma-Aldrich were of analytical grade and used without further purification. Cobalt (II) chloride's hexahydrate ($CoCl_2$ x $6H_2O$, 98%) and ferric (III) chloride hexahydrate ($FeCl_3$ x $6H_2O$, >97%) were used as reactants.

According to our previous reports [12,13], the process for elaborating the Co@α-Fe_2O_3 powder was carried out in multiple steps. The freshly isolated ovalbumin was homogenized under vigorous agitation with bi-distilled water for 30 min to obtain a homogeneous solution. Then, 2.703 g of $FeCl_3$ x $6H_2O$ and 1.189 g of $CoCl_2$ x $6H_2O$ (with a Co/Fe ratio equal to 0.5) were dissolved together in a small amount of distilled water to get a clear solution. The solution

containing Fe^{3+} and Co^{2+} ions was added dropwise to the ovalbumin solution without pH adjustment. The resultant mixture was heated on a hot plate at 80 °C for 2 hours with continuous stirring. The suspension was then filtered and thoroughly rinsed on multiple occasions.

To identify the different crystalline phases present in the Co@α-Fe_2O_3, a Shimadzu 6100 Diffractometer, with Cu Kα radiation (λ = 1.54056 Å) operating at 40 kV, was used. The XRD pattern was recorded over a range of 20 to 70° with a step scan of 0.02°. The unit cell volume and lattice parameters of the synthesized Co@α-Fe_2O_3 nanopowder were estimated from XRD data using the Rietveld refinement approach integrated into the FullProf Suite software. The FTIR spectrum of the prepared Co@α-Fe_2O_3 was recorded with a spectrophotometer scanning a wavenumber range of 350 to 4000 cm^{-1}. The SEM and EDX analysis (operating voltage of 15kV) were employed to investigate the morphology and crystalline nature of the sample.

3. Results and Discussion

The XRD pattern of the synthesized Co@α-Fe_2O_3 nanoparticles is displayed in Figure 2. The refraction spectra of (012), (104), (110), (113), (024), (116), (214) and (300) planes are all compatible with the rhombohedral (hexagonal) phase of hematite α-Fe_2O_3 NPs (JCPDS card N°. 33–0664), appearing at 2θ = 24.06°, 33.07°, 35.57°, 40.75°, 49.32°, 53.94°, 62.38°, and 63.89°, respectively. The two weak peaks that emerged at 2θ = 30.05° and 43.18° correspond to the d-values of the (220) and (400) reflections, respectively, in the standard JCPDS card N°: 39-1346 of the maghemite (γ-Fe_2O_3) phase [14]. Quantitative phase analysis was performed using the most intense non-overlapping XRD peaks for each phase: the (104) plane for α-Fe_2O_3 and (220) for γ-Fe_2O_3. The calculated phase fractions were found to be 94% for α-Fe_2O_3 and 6% for γ -Fe_2O_3. The coexistence of α and γ phases may impact magnetic and catalytic behavior. Similar results have been reported in the literature [15,16].

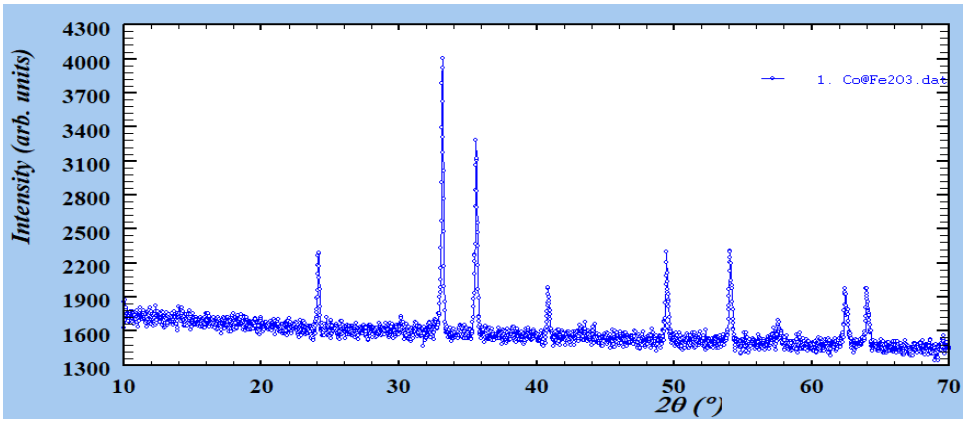

Figure 2. XRD pattern of the prepared Co@α-Fe_2O_3.

The Debye–Scherrer formula was used to determine the average crystallite size [17]:

$$L = \frac{0.9\,\lambda}{\beta\,\cos\theta} \quad (1)$$

Where β, θ, and λ correspond to the full-width at half maximum (FWHM) intensity, Bragg's angle, and wavelength of X-ray radiation (Cu K_α radiation equals 1.54056 Å), respectively. It is important to note that, in XRD patterns, the FWHM of peaks at low angles is more significant in estimating the grain size. Therefore, the most intense peak, corresponding

to the (104) plane, was used to compute the nanoparticles' size. According to the preceding data, the average size of the Co@α-Fe_2O_3 nanoparticles was estimated to be 45 nm.

The Rietveld refinement analysis employs multiple mathematical computations in the refinement process, which have been previously described in previous studies [18–20]. In this work, we provide a brief description of the analysis performed on the experimental powder diffraction data. The crystal structure of the elaborated sample was characterized using the Rietveld global profile fitting approach in FullPROF[21].

The experimental diffraction profiles were refined with the most suitable pseudo-Voigt function (pVF). The B(2θ) line broadening function, for the $K_{\alpha 1}$ and $K_{\alpha 2}$ profiles, can be described by the pVF combination as follows:

$$pV(x) = \eta\, L(x) + (1 - \eta)\, G(x) \qquad (2)$$

Where η denotes the Lorentzian contribution, whereas the functions G(x) and L(x) represent the Gaussian and Lorentzian parts, respectively, the main objective of the refinement step is to minimize the difference between the simulated or calculated pattern and the experimental or observed pattern. For this purpose, Marquardt's least-squares methods were used, assuming that the structural parameters depend only on the integrated peak intensities. To assess the minimization process (refinement), the reliability index parameters were used, including residuals for the Bragg factor R_{Bragg}, pattern Rp, weighted pattern Rwp, structure factor R_F, and goodness of fit χ^2. These factors were utilized to evaluate the goodness of fit (GOF) of the calculated pattern to the observed data, as represented by the following relations [22].

$$R_B = \frac{\sum_i |I_{i(obs)} - I_{i(cal)}|}{\sum_i I_{i(obs)}} . 100 \qquad (3)$$

$$R_p = \frac{\sum_i |y_{i(obs)} - y_{i(cal)}|}{\sum_i y_{i(obs)}} . 100 \qquad (4)$$

$$R_{wp} = \left[\frac{\sum_i w_i (y_{i(obs)} - y_{i(cal)})^2}{\sum_i w_i y_{i(obs)}^2}\right]^{\frac{1}{2}} . 100 \qquad (5)$$

$$R_{exp} = \left[\frac{(N+P+C)}{\sum_i w_i y_{i(obs)}^2}\right]^{\frac{1}{2}} . 100 \qquad (6)$$

$$\chi^2 = \left[\frac{R_{wp}}{R_{exp}}\right]^2 . 100 \qquad (7)$$

Where N, P, C, and I denote the number of experimental observations, the number of fitting parameters, the number of constraints, and the integrated intensity, respectively. Moreover, $y_i(cal)$ and $y_i(obs)$ represent the calculated and experimental intensities at step i, while $w_i = (1/y_i(obs))$ corresponds to the weight of experimental observations. The goodness of fit (GOF) indicator is calculated from R_{wp} and R_{exp} values as follows:

$$GOF = \frac{R_{wp}}{R_{exp}} \qquad (8)$$

The process of Rietveld refinement, which utilizes the XRD Pattern, is used to improve the XRD data. For the first refinement cycle, the atomic positions documented in the previous study [23] were used. The Thompson pV symmetry function was applied to represent the peak profile function. The Cobalt (Co) atomic positions were fixed to be the same as those of iron (Fe) during the refinement. The refinement procedure began by refining: the scale factor, zero

point of the detector with lattice parameters, atomic positions, and other main Rietveld refining variables. This process was repeated iteratively until the χ^2 factor reached its minimum possible value. The Rietveld refinement parameters and the Wyckoff positions for Co@α-Fe_2O_3 are presented in Tables 1 and 2. As shown in Table 2, the site occupancy (Occ) for Cobalt is recorded at 0.11111, confirming its integration into the α-Fe_2O_3 lattice at the same Wyckoff sites as the Fe atoms. The experimental and calculated diffraction patterns are depicted in Figure 3.

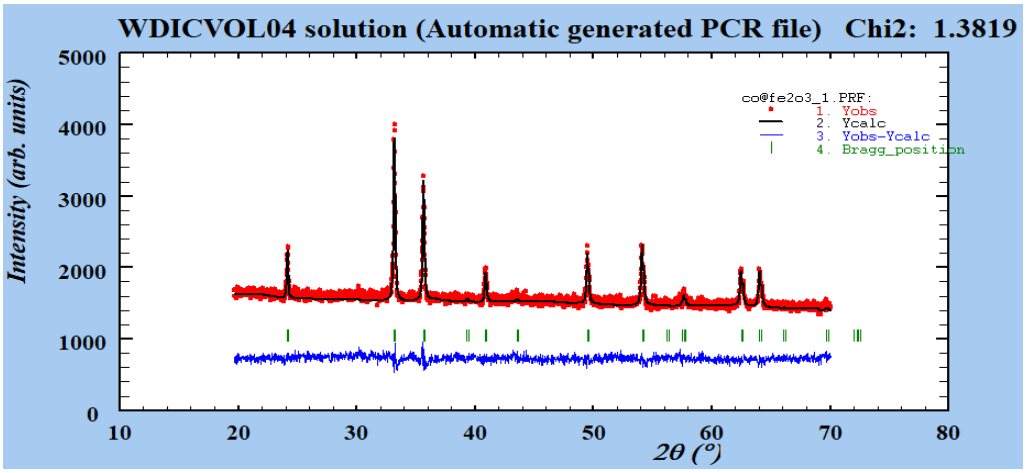

Figure 3. Final Rietveld refinement of Co@α-Fe_2O_3: experimental (red dots) XRD pattern, calculated pattern (black line), and difference profile curve (blue).

Table 1. Space Group Information and Rietveld refinement parameter obtained for Co@α-Fe_2O_3.

Unit cell parameters	**a = b = 5,0326 Å; c = 13,7359 Å, α = β = 90°; γ = 120°**
Number of Space Groups	167
Hermann-Manguin symbol	R -3 c
Crystal System	Trigonal
Laue Class	-3m1
General multiplicity	36
Centrosymmetry	Centric (-1 at origin)
sVolume (Å^3)	V = 301.28
Bragg R-factor	R_{Bragg} = 23.1
Rf – factor	R_F = 24.1
R factors	R_P = 2.31, R_{WP} = 2.90
Chi-squared χ^2	χ^2 = 1.38

Table 2. Wyckoff positions for Co@α-Fe_2O_3.

Atom	**Mult**	**x/a**	**y/b**	**z/c**	**B**	**Occ**
O	18	0.00000	0.31269	0.25000	0.49763	0.47261
Fe	12	0.00000	0.00000	0.35521	1.00000	0.22222
Co	12	0.00000	0.00000	0.35521	1.00000	0.11111

To determine the hematite structure, a rhombohedral symmetry was applied. The axis ratio c/a of hematite was determined to be 2.73, confirming the shortening of this ratio along the c-axis, as reported in the literature, where the ideal value is 2.83 [24]. In the structure, iron (Cobalt) atoms are surrounded by oxygen atoms in an octahedral arrangement, with the oxygen atoms slightly rotated in relation to each other. Table 3 shows the interatomic distance of Fe(Co)—Fe(Co) values and bond lengths of Fe(Co)—O values in the structure of Co@α-Fe_2O_3. The crystallite size obtained from the Rietveld analysis (64 nm) is slightly larger than that estimated by Scherrer's formula (45 nm). This observed difference could be attributed to the Scherrer model, which does not account for internal effects and which fits peak shapes using only the Gaussian function. In contrast, the pseudo-Voight function pVF is used to fit the shape of the peaks' profile, combining both Lorentzian (microstrain) and Gaussian (crystallite size) functions.

Table 3. Crystallite size and bond length.

Crystalline size (nm)		M = Fe or Co			
Scherrer's formula	**Rietveld analysis**	**M-O (Å)**	**M-O (Å)**	**M-$M_{(A)}$ (Å)**	**M-$M_{(B)}$ (Å)**
45	64	1.926	2.137	2.89	3.70

In the structure of Co@α-Fe_2O_3, there are two types of metal atoms with unequal Fe(Co)—Fe(Co) distance along the hexagonal c-axis labeled as: Type A ($d_{Fe—Fe}$ = 2.89 Å) and Type B ($d_{Fe—Fe}$ = 3.70 Å). Each metal atom is coordinated by six oxygen atoms arranged in two equilateral triangles. Three oxygen atoms are positioned above the central Fe(Co) atom, with an M–O bond length of 2.137 Å, while the other three are located below with a slightly shorter M–O length of 1.926 Å. Polfus et al. reported similar results, with Fe-O bond length ranging from 1.9 to 2.14 Å [25]. The structural geometry of Co@α-Fe_2O_3 is presented in Figure 4.

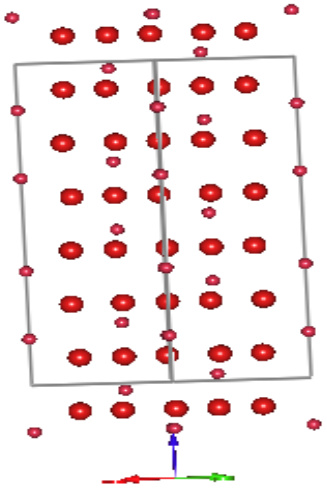

Figure 4. Structural geometry of Co@α-Fe_2O_3 NPs.

The FTIR spectrum in Figure 5 depicts distinct absorption bands at 519 and 440 cm^{-1}, characteristic of the α-Fe_2O_3 phase, which represent the metal-oxygen Fe —O stretching vibrations. The band at 519 cm^{-1} could be attributed to metal-oxygen O—Fe —O (ν_1) deformation in both tetrahedral and octahedral sites, while the band at 440 cm^{-1} could be associated with the metal-oxygen deformation (ν_2) in the octahedral site of the α-Fe_2O_3 structure [26,27]. Furthermore, the bands situated at 1040 and 1120 cm^{-1} arise from the crystalline Fe–O vibrational modes, which are the characteristics of the structure of hematite α-Fe_2O_3 [28].

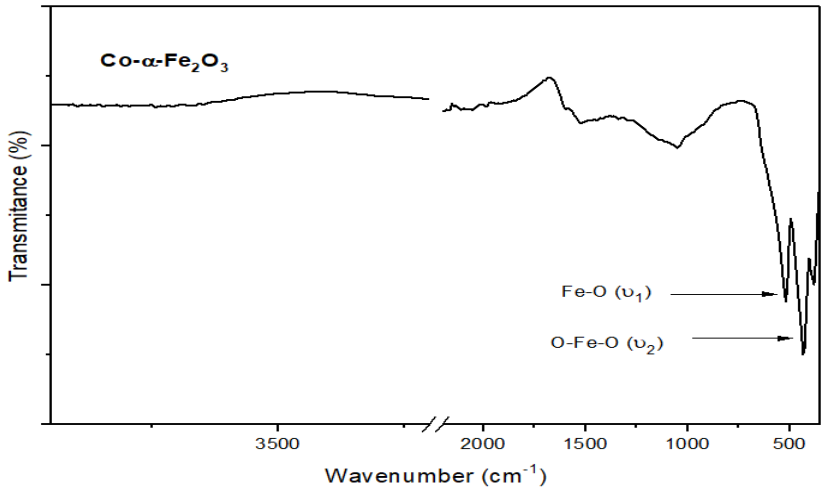

Figure 5. FTIR spectra of Co@α-Fe_2O_3 nanoparticles.

SEM /EDX analysis was carried out to investigate the morphology and structural characteristics of the samples. Microscopic observations of the sample reveal that Co-doped hematite crystallites do not have a regular, uniform shape and tend to form agglomerates with a non-uniform distribution of grains, exhibiting nanometric, inhomogeneous sizes. The EDX spectrum of Co@α-Fe_2O_3 reveals the presence of Fe, O, and Co (Figure 6), confirming the formation of the Co@α-Fe_2O_3 the presence of Fe, O, and Co.

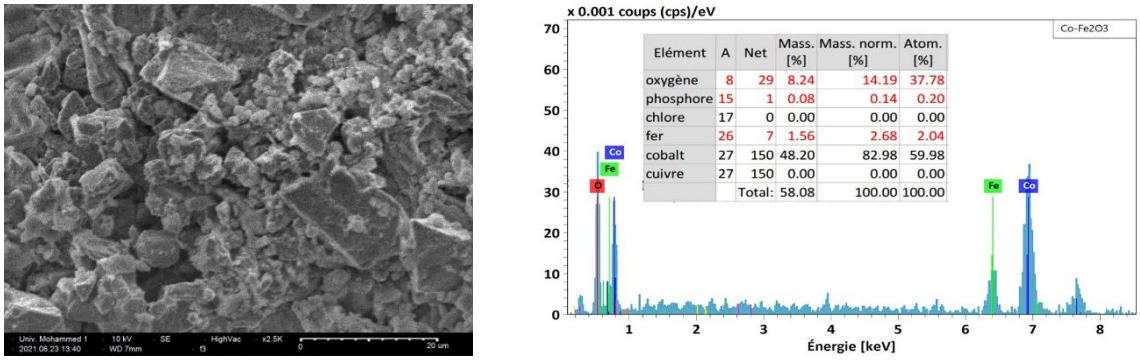

(a) **(b)**

Figure 6. (a) SEM image; **(b)** EDX spectrum of prepared Co@α-Fe_2O_3 NPs.

4. Conclusions

Cobalt-doped iron oxide (Co@α-Fe_2O_3) nanoparticles were successfully prepared using a simple and low-cost egg white-assisted method. The main phase was α-Fe_2O_3, with a small amount of γ-Fe_2O_3 impurity, and Cobalt incorporation was confirmed by EDX and FTIR analyses. The refined unit-cell parameters were determined as follows: a=b=5.0326 Å, c=13.7358 Å, and unit-cell V=301.28 $Å^3$. Some particle agglomeration was observed, which may affect their properties. Despite these limitations, the nanoparticles show promise for applications in catalysis and sensors. In future work, we will investigate the impact of Cobalt insertion on the photocatalytic performance of Co@α-Fe_2O_3 to explore its potential for environmental and energy applications.

Author Contributions

Conceptualization, B.C.E.; methodology, M.E. and S.H.; software, S.H.; validation, B.C.E.; formal analysis, M.B.; investigation, S.H. and M.B.; resources, B.S.; data curation, M.B.; writing—original draft preparation, B.C.E. and A.E.; writing—review and editing, A.E.; visualization, B.S.; supervision, B.C.E. All authors have read and agreed to the published version of the manuscript. All authors have read and agreed to the published version of the manuscript.

Institutional Review Board Statement

Not applicable.

Informed Consent Statement

Not applicable.

Data Availability Statement

Data supporting the findings of this study are available upon reasonable request from the corresponding author.

Funding

This research received no external funding.

Acknowledgments

Declared none.

Conflicts of Interest

The authors declare no conflict of interest.

References

1. Saleem, S.; Ashiq, M.N.; Manzoor, S.; Ali, U.; Liaqat, R.; Algahtani, A.; Mujtaba, S.; Tirth, V.; Alsuhaibani, A.M.; Refat, M.S.; Ali, A.; Aslam, M.; Zaman, A. Analysis and characterization of opto-electronic properties of iron oxide (Fe_2O_3) with transition metals (Co, Ni) for the use in the photodetector application. *J. Mater. Res. Technol.* **2023**, *25*, 6150-6166, https://doi.org/10.1016/j.jmrt.2023.07.065.
2. Gupta, R.; Polaka, S.; Rajpoot, K.; Tekade, M.; Sharma, M.C.; Tekade, R.K. Chapter 6 - Importance of toxicity testing in drug discovery and research. In Pharmacokinetics and Toxicokinetic Considerations; Tekade, R.K., Ed.; Academic Press: **2022**; Volume 2, pp. 117-144, https://doi.org/10.1016/B978-0-323-98367-9.00016-0.
3. Hublikar, L.V.; Ganachari, S.V.; Patil, V.B. Zn and Co ferrite nanoparticles: towards the applications of sensing and adsorption studies. *Environ. Sci. Pollut. Res.* **2023**, *30*, 66994-67007, https://doi.org/10.1007/s11356-023-27201-z.
4. Rajapandi, P.; Viruthagiri, G. Probing analysis of Cu-doping on the structural, optical, morphological and magnetic properties of hematite nanoparticles and their antibacterial activity. *Spectrochim. Acta A Mol. Biomol. Spectrosc.* **2024**, *305*, 123471, https://doi.org/10.1016/j.saa.2023.123471.
5. Mala, N.A.; Rather, M.u.D.; Ali, R.N.; Hussain, S.; Ibrahim, S.M.; Ullah, N.; Husain, S.; Ahmad, Z. Unravelling the structure and electrochemical performance of Mo–Cu dual-doped NiO nanorod shaped electrodes for supercapacitor application. *Int. J. Hydrogen Energy* **2023**, *48*, 32739-32755, https://doi.org/10.1016/j.ijhydene.2023.05.068.
6. Kamal, A.; Razia, E.T.; Zahra, M.; Sardar, S.; Mumtaz, A. Monitoring the synergistic effect of Mn/Ni Co-doping and morphological engineering in α-Fe_2O_3 for energy storage capacity as battery type electrode material. *Int. J. Hydrogen Energy* **2024**, *88*, 1280-1292, https://doi.org/10.1016/j.ijhydene.2024.09.259.
7. Paúl-Navarrón, M.; Lloreda-Jurado, P.J.; Chicardi, E.; Balu, K.; Dieuzeide, M.L.; Tejeda, R.; Avendaño, R.; Sepúlveda, R. Development and characterization of Fe_2O_3 nanoparticles doped with Al_2O_3 / TiO_2 for green hydrogen production. *Ceram. Int.* **2025**, *51*, 6579-6586, https://doi.org/10.1016/j.ceramint.2024.12.102.
8. Sakurai, S.; Namai, A.; Hashimoto, K.; Ohkoshi, S.-i. First Observation of Phase Transformation of All Four Fe_2O_3 Phases (γ → ε → β → α-Phase). *J. Am. Chem. Soc.* **2009**, *131*, 18299-18303, https://doi.org/10.1021/ja9046069.
9. Huda, M.N.; Walsh, A.; Yan, Y.; Wei, S.-H.; Al-Jassim, M.M. Electronic, structural, and magnetic effects of 3d transition metals in hematite. *J. Appl. Phys.* **2010**, *107*, 123712, https://doi.org/10.1063/1.3432736.
10. Tamirat, A.G.; Rick, J.; Dubale, A.A.; Su, W.-N.; Hwang, B.-J. Using hematite for photoelectrochemical water splitting: a review of current progress and challenges. *Nanoscale Horiz.* **2016**, *1*, 243-267, https://doi.org/10.1039/c5nh00098j.
11. Naveas, N.; Pulido, R.; Marini, C.; Hernández-Montelongo, J.; Silván, M.M. First-principles calculations of hematite (α-Fe_2O_3) by self-consistent DFT+U+V. *iScience* **2023**, *26*, 106033, https://doi.org/10.1016/j.isci.2023.106033.

12. Hmamouchi, S.; El Yacoubi, A.; El Idrissi, B.C. Using egg ovalbumin to synthesize pure α-Fe_2O_3 and cobalt doped α-Fe_2O_3: structural, morphological, optical and photocatalytic properties. *Heliyon* **2022**, *8*, e08953, https://doi.org/10.1016/j.heliyon.2022.e08953.
13. Hmamouchi, S.; Yacoubi, A.E.; Hezzat, M.E.; Sallek, B.; Idrissi, B.C.E. α-Fe_2O_3/g-C_3N_4 nanocomposite with type II heterojunction for methylene blue photodegradation. *Chem. Phys. Impact* **2024**, *8*, 100577, https://doi.org/10.1016/j.chphi.2024.100577.
14. Byeon, H.; Kumar Lautre, H.; Rajagopalan, N.R.; Sivaprakash, M.; Kiradoo, G.; Haile, A.; Arul Raja, R.A.; Sunil, J. Facile preparation of Fe_2O_3 catalyst and assessment of its photodegradation performance for industrial effluent purification. *Results Chem.* **2024**, *7*, 101435, https://doi.org/10.1016/j.rechem.2024.101435.
15. Suresh, R.; Giribabu, K.; Manigandan, R.; Mangalaraja, R.V.; Solorza, J.Y.; Stephen, A.; Narayanan, V. Synthesis of Co^{2+}-doped Fe_2O_3 photocatalyst for degradation of pararosaniline dye. *Solid State Sci.* **2017**, *68*, 39-46, https://doi.org/10.1016/j.solidstatesciences.2017.04.005.
16. Sharfalddin, A.; Alzahrani, E.; Alamoudi, M. Micro, Sono, Photocatalytic Degradation of Eosin B Using Ferric Oxide Doped with Cobalt. *Chem. Sci. Int. J.* **2016**, *13*, 1-13, https://doi.org/10.9734/ACSJ/2016/23648.
17. Akhter, M.; Kaunsar, R. Hydrothermal Synthesis and Characterization of Iron Oxide Nanoparticles. *J. Recent Adv. Nanomed. Nanotech.* **2025**, *1*, 555562.
18. Paufler, P. R. A. Young (ed.). The Rietveld Method. International Union of Crystallography. Oxford University Press 1993. 298 p. Price £ 45.00. ISBN 0–19–855577–6. *Cryst. Res. Technol.* **1995**, *30*, 494-494, https://doi.org/10.1002/crat.2170300412.
19. El Yacoub, A.; Massit, A.; El Moutaoikel, S.; Rezzouk, A.; El Idrissi, B.C. Rietveld Refinement of the Crystal Structure of Hydroxyapatite Using X-ray Powder Diffraction. *Am. J. Mater. Sci. Eng.* **2017**, *5*, 1–5, https://doi.org/10.12691/AJMSE-5-1-1.
20. Pradhan, S.K.; Bid, S.; Gateshki, M.; Petkov, V. Microstructure characterization and cation distribution of nanocrystalline magnesium ferrite prepared by ball milling. *Mater. Chem. Phys.* **2005**, *93*, 224-230, https://doi.org/10.1016/j.matchemphys.2005.03.017.
21. Rodríguez-Carvajal, J. Recent advances in magnetic structure determination by neutron powder diffraction. *Physica B: Condens. Matter* **1993**, *192*, 55-69, https://doi.org/10.1016/0921-4526(93)90108-I.
22. Young, R.A.; Wiles, D.B. Application of the Rietveld Method for Structure Refinement with Powder Diffraction Data. *Adv. X-Ray Anal.* **1980**, *24*, 1-23, https://doi.org/10.1154/S0376030800007114.
23. De Los Santos Valladares, L.; Bustamante Domínguez, A.; León Félix, L.; Kargin, J.B.; Mukhambetov, D.G.; Kozlovskiy, A.L.; Moreno, N.O.; Flores Santibañez, J.; Castellanos Cabrera, R.; Barnes, C.H.W. Characterization and magnetic properties of hollow α-Fe_2O_3 microspheres obtained by sol gel and spray roasting methods. *J. Sci. Adv. Mater. Devices* **2019**, *4*, 483-491, https://doi.org/10.1016/j.jsamd.2019.07.004.
24. Justus, J.S.; Dharma Roy, S.D.; Saravanakumar, K.; Ezhil Raj, A.M. Judging phase purity of hematite (*α*-Fe_2O_3) nanoparticles through structural and magnetic studies. *Mater. Res. Express* **2021**, *8*, 055005, https://doi.org/10.1088/2053-1591/abff09.
25. Polfus, J.M.; Jayasayee, K. Robust nanocomposites of α-Fe_2O_3 and N-doped graphene oxide: Interfacial bonding and chemisorption of H_2O. *Carbon* **2019**, *152*, 497-502, https://doi.org/10.1016/j.carbon.2019.05.033.
26. Bozkurt, G. Synthesis and Characterization of α-Fe_2O_3 Nanoparticles by Microemulsion Method. *Erzincan Univ. J. Sci. Technol.* **2020**, *13*, 890-897, https://doi.org/10.18185/erzifbed.742160.
27. Karrab, A.; Bensimon, R.; Muller-Bouvet, D.; Bastide, S.; Cachet-Vivier, C.; Ammar, S. Nanostructured « Fe_2O_3/nickel-based co-catalyst» electrode materials for the photoelectrochemical oxidation of urea in wastewaters. *Appl. Phys. A* **2022**, *128*, 1067, https://link.springer.com/article/10.1007/s00339-022-06221-5.
28. Satheesh, R.; Vignesh, K.; Suganthi, A.; Rajarajan, M. Visible light responsive photocatalytic applications of transition metal (M=Cu, Ni and Co) doped α-Fe_2O_3 nanoparticles. *J. Environ. Chem. Eng.* **2014**, *2*, 1956-1968, https://doi.org/10.1016/j.jece.2014.08.016.

Publisher's Note & Disclaimer